*Inorg. Chem.* **2004**, *43*, 4974–4987


# Investigation of the Electronic and Structural Properties of Potassium Hexaboride, $KB_6$, by Transport, Magnetic Susceptibility, EPR, and NMR Measurements, Temperature-Dependent Crystal Structure Determination, and Electronic Band Structure Calculations

**A. Ammar, M. Ménétrier, A. Villesuzanne, S. Matar, B. Chevalier, and J. Etourneau***

*Institut de Chimie de la Matière Condensée de Bordeaux, ICMCB-CNRS, 87 Avenue du Dr. A. Schweitzer, 33608 Pessac Cedex, France*

**G. Villeneuve**

*CRP2A, UMR 5060, CNRS-IRAMAT, Université Bordeaux 3, 33607 Pessac Cedex, France*

**J. Rodríguez-Carvajal**

*Laboratoire Léon Brillouin (CEA-CNRS), CEA/Saclay (CEA/DSM/DRECAM/LLB), 91191 Gif-sur-Yvette Cedex, France*

**H.-J. Koo**

*Department of Chemistry, Kyung Hee University, Seoul, South Korea 130-701*

**A. I. Smirnov and M.-H. Whangbo***

*Department of Chemistry, North Carolina State University, Raleigh, North Carolina 27695-8204*

Received April 29, 2004

The electronic and structural properties of potassium hexaboride, $KB_6$, were examined by transport, magnetic susceptibility, EPR, and NMR measurements, temperature-dependent crystal structure determination, and electronic band structure calculations. The valence bands of $KB_6$ are partially empty, but the electrical resistivity of $KB_6$ reveals that it is not a normal metal. The magnetic susceptibility as well as EPR and NMR measurements show the presence of localized electrons in $KB_6$. The EPR spectra of $KB_6$ have two peaks, a broad ($\sim$320 G) and a narrow (less than $\sim$27 G) line width, and the temperature-dependence of the magnetic susceptibility of $KB_6$ exhibits a strong hysteresis below 70 K. The temperature-dependent crystal structure determination of $KB_6$ shows the occurrence of an unusual variation in the unit cell parameter hence supporting that the hysteresis of the magnetic susceptibility is a bulk phenomenon. The line width $\Delta H_{pp}$ of the broad EPR signal is independent of temperature and EPR frequency. This finding indicates that the line broadening results from the dipole–dipole interaction, and the spins responsible for the broad EPR peak has the average distance of $\sim$1.0 nm. To explain these apparently puzzling properties, we examined a probable mechanism of electron localization in $KB_6$ and its implications.

## 1. Introduction

Borides of alkali-metal, alkaline-earth, and rare-earth elements possess two-dimensional (2D) and three-dimensional (3D) electron-deficient boron networks and exhibit interesting physical properties.[1−6] The magnesium diboride $MgB_2$ consists of honeycomblike 2D boron networks and becomes a superconductor at a rather high temperature ($T_c$ = 40 K).[7−10] The hexaborides $AB_6$ (A = alkali metal, alkaline earth, rare earth, actinide) have 3D boron networks

* Authors to whom correspondence should be addressed. E-mail: jean.etourneau@icmcb.u-bordeaux.fr (J.E.); mike_whangbo@ncsu.edu (M.-H.W.).

(1) Blum, P.; Bertaut, F. *Acta Crystallogr.* **1954**, *7*, 81.
(2) Naslain, R.; Etourneau, J. *C. R. Acad. Sc.* **1966**, *263*, 484.
(3) Etourneau, J.; Naslain, R. *J. Less-Common Met.* **1971**, *24*, 183.
(4) Etourneau, J. In *Inorganic Reactions and Methods*; Zuckerman, J. J., Hagen, A. P., Eds.; VCH: New York, 1991; Vol. 13, pp 167−196.



10.1021/ic049444c CCC: $27.50 
Published on Web 07/07/2004

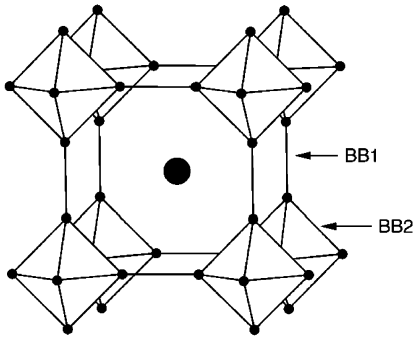


**Figure 1.** Schematic perspective view of the crystal structure of $AB_6$, where the small dots refer to the B atoms and the large filled circle refers to the A cation. BB1 and BB2 are the inter- and intraoctahedron B−B bonds, respectively.

made up of $B_6$ octahedra,[2,11−14] in which the $A^{n+}$ ($n = 1-4$) cations and $(B_6)^{n-}$ octahedral clusters adopt the CsCl-type structure (Figure 1). Each $B_6$ octahedron is linked to the surrounding six $B_6$ octahedra by its vertexes to form six B−B bonds so that there occur two kinds of B−B distances. The alkaline-earth and rare-earth hexaborides $AB_6$ (A = Ca, Sr, Ba, Eu, Yb) have 20 valence electrons/formula unit (FU). These hexaborides are either small gap semiconductors or semimetals.[12,15−22] Thus, if electron localization is neglected,[23−25] one would expect from the rigid band picture that the rare-earth and actinide hexaborides $AB_6$ (A = Y, Ln, Th) with 21 valence electrons/FU are metals, and so is the alkali-metal hexaboride $KB_6$ with 19 valence electrons/FU. Indeed, $YB_6$ and $LaB_6$ are metals and exhibit superconductivity at low temperatures (i.e., $T_c = 7.1$ and 0.45 K, respectively).[13,26] An electronic band structure study[27] suggests that the Fermi level of $KB_6$ lies well below the top of the valence band, as expected from the rigid band picture. Our electrical resistivity measurements of $KB_6$ carried out for pellets of fine powder samples indicated that $KB_6$ is not a normal metal.[28] Moreover, our magnetic susceptibility and EPR measurements showed that $KB_6$ has localized spins and exhibits a highly unusual hysteresis in the magnetic susceptibility below 100 K.[28] These puzzling observations are difficult to understand if $KB_6$ is a normal metal. In this work we probe these observations on the basis of physical property measurements (i.e., electrical resistivity, magnetic susceptibility, EPR, NMR), temperature-dependent crystal structure determination, and electronic band structure calculations.

Our work is organized as follows: Section 2 summarizes sample preparation. Results of physical property measurements (electrical resistivity, magnetic susceptibility, EPR, NMR, and SEM) are described in section 3, and those of temperature-dependent crystal structure determination in section 4. The orbital compositions of the valence and conduction bands of $KB_6$ are analyzed in section 5 on the basis of first principles and tight-binding calculations. How to account for electron localization in $KB_6$ and its consequence on the magnetic properties are discussed in section 6. Finally, important conclusions of our work are summarized in section 7.

## 2. Synthesis of $KB_6$

Powder samples of $KB_6$ were prepared by direct synthesis from amorphous boron (99.99% purity, particle size <150 nm, from Alfa Aesar, Johnson Matthey GmbH) and potassium metal (Sigma-Aldrich, purity >99.9% after distillation). The chemical reaction was carried out with potassium excess in sealed molybdenum crucible at 900 °C for 2 days under pure argon atmosphere. After opening of the molybdenum crucible under pure argon atmosphere in a drybox, the excess potassium that did not react was removed by distillation under vacuum ($10^{-7}$ mbar) at 350 °C for 2 days. The final product was washed in 5 N hydrochloric acid at 75 °C for 5 h and then with pure ethyl alcohol. The final product was dried under vacuum ($10^{-7}$ mbar) at room temperature. We determined by inductively coupled plasma (ICP) spectroscopy and Rietveld refinements (Table 1) that these $KB_6$ samples are slightly potassium deficient.

Samples showing compositions ranging from $KB_6$ to $K_{0.96}\square_{0.04}B_6$ are "Bordeaux" red, and those farther from stoichiometry ($0.84 < x < 0.96$) are rather black. Single phases are observed for $0.84 \leq x \leq 1$. The composition depends on the synthesis temperature, ranging between 800 and 1050 °C. The lower the synthesis temperature, the greater the potassium content becomes. A scanning electron microscopy (SEM) picture of powder $K_{0.97}B_6$ is presented in Figure 2, which shows cubic single crystals with an average side length smaller than 70 nm.

(5) Blomberg, M. K.; Merisalo, M. J.; Korsukova, M. M.; Gurin, V. N. *J. Alloys Compd.* **1995**, *217*, 23.
(6) Matar, S. F.; Etourneau, J. *Int. J. Inorg. Mater.* **2000**, *2*, 43.
(7) Nagamutsu, J.; Nakagawa, N.; Muranaka, T.; Zenitani, Y.; Akimitsu, J. *Nature* **2001**, *410*, 63.
(8) Bud'ko, S. L.; Lapertot, G.; Petrovic, C.; Cunningham, C. E.; Anderson, N.; Canfield, P. C. *Phys. Rev. Lett.* **2001**, *86*, 1877.
(9) Kortus, J.; Mazin, I. U.; Belashchenko, K. D.; Andropov, V. P.; Boyer, L. L. *Phys. Rev. Lett.* **2001**, *86*, 4656.
(10) An, J. M.; Pickett, W. E. *Phys. Rev. Lett.* **2001**, *86*, 4366.
(11) Ott, H. R.; Chernokov, M.; Felder, E.; Digiorgi, L.; Moshopoulou, E. G.; Sarrao, J. L.; Fisk, Z. *Z. Phys. B* **1997**, *102*, 83.
(12) Schmitt, K.; Stückl, C.; Ripplinger, H.; Albert, B. *Solid State Sci.* **2001**, *3*, 321.
(13) Takahashi, Y.; Oshima, K.-I.; Okamura, F. P.; Otani, S.; Tanaka, T. *J. Phys. Soc. Jpn.* **1999**, *68*, 2304 and references therein.
(14) Etourneau, J. Ph.D. Thesis, University of Bordeaux, 1970. Etourneau, J.; Naslain, R.; Laplaca, S. *J. Less Common Met.* **1971**, *24*, 183.
(15) Longuet-Higgins, H. C.; de V. Roberts, M. *Proc. R. Soc. A* **1954**, *224*, 336.
(16) Etourneau, J.; Mercurio, J. P.; Naslain, R.; Hagenmuller, P. *J. Solid State Chem.* **1970**, *2*, 332.
(17) Tarascon, J. M.; Etourneau, J.; Dordor, P.; Hagenmuller, P.; Kasaya, M.; Coey, J. M. D. *J. Appl. Phys.* **1980**, *51*, 574.
(18) Massidda, S.; Continenza, A.; Pascale, T. M.; Monnier, R. *Z. Phys. B* **1997**, *102*, 83.
(19) Degiorgi, L.; Felder, E.; Ott, H. R.; Sarrao, J. L.; Fisk, Z. *Phys. Rev. Lett.* **1997**, *79*, 5134.
(20) Werheit, H.; Au, T.; Schmechel, R.; Paderno, Y. B.; Konovalova, E. S. *J. Solid State Chem.* **2000**, *154*, 87.
(21) Deninger, J. D.; Clack, J. A.; Allen, J. W.; Gweon, G.-H.; Poirier, D. M.; Olson, C. G.; Sarrao, J. L.; Bianchi, A. D.; Fisk, Z. *arXive: cond-mat*/0107429.
(22) Tromp, H. J.; van Gelderen, P.; Kelly, P. J.; Brocks, G.; Bobbert, P. A. *Phys. Rev. Lett.* **2001**, *87*, 16401.
(23) Mott, N. F. *Metal−Insulator Transitions*, 2nd ed.; Taylor & Francis: New York, 1990.
(24) Hayes, W.; Stoneham, A. M. *Defects and Defect Processes in Nonmetallic Solids*; Wiley: New York, 1985.
(25) (a) Chaktraverty, B. K.; Schlenker, C.; Marezio, M. *J. Phys., Colloq.* **1976**, 353. (b) Chaktraverty, B. K. *Philos. Mag. B* **1980**, *42*, 473.
(26) Shell, G.; Winter, H.; Tietschel, H.; Gompf, F. *Phys. Rev. B* **1982**, *25*, 1589 and references therein.
(27) Okatov, S. V.; Ivanovskii, A. L. *Phys. Status Solidi B* **2000**, *222*, R6.
(28) Etourneau, J.; Ammar, A.; Villesuzanne, A.; Villeneuve, G.; Chevalier, B.; Whangbo, M.-H. *Inorg. Chem.* **2003**, *42*, 4242.

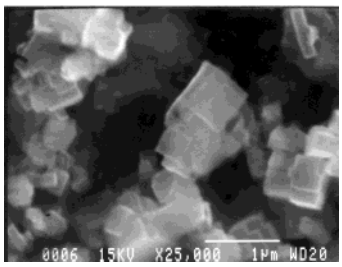


**Figure 2.** SEM picture of $K_{0.97}B_6$.

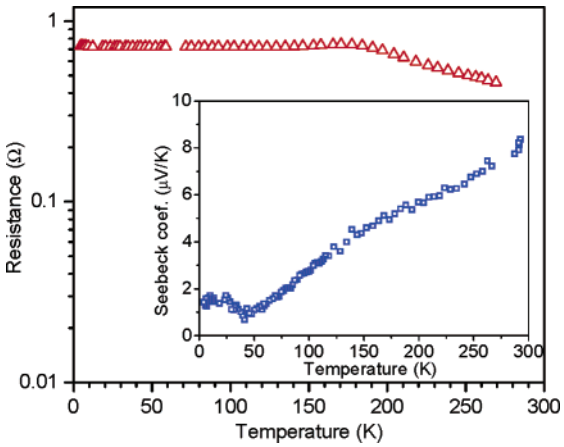


**Figure 3.** Electrical resistance and thermoelectric power (inset) of $K_{0.97}B_6$ as a function of temperature.

**Table 1.** Temperature Dependence of the Structural Parameters of $KB_6$

| temp (K) | *x*(B) | cell param (Å) | K-occupation |
|---|---|---|---|
| 25.00 | 0.300 84(34) | 4.221 57(5) | 0.9447(44) |
| 35.00 | 0.302 11(97) | 4.221 85(10) | * |
| 45.00 | 0.302 79(85) | 4.222 38(10) | * |
| 48.00 | 0.301 54(59) | 4.221 77(5) | * |
| 55.00 | 0.301 68(59) | 4.221 61(5) | * |
| 60.00 | 0.301 04(25) | 4.220 98(2) | 0.9464(33) |
| 75.00 | 0.301 80(*) | 4.221 89(15) | * |
| 100.00 | * | 4.222 07(10) | * |
| 150.00 | * | 4.222 47(10) | * |
| 200.00 | * | 4.223 04(10) | * |
| 250.00 | * | 4.223 71(15) | * |
| 300.00 | 0.301 83(45) | 4.224 60(5) | 0.9469(82) |

* Undetermined due to lack of enough reflections.

## 3. Physical Properties

**3.1. Electrical Resistivity and Thermoelectric Power.** The electrical resistance measured for pressed pellets of $K_{0.97}B_6$ samples (sintered under saturation vapor pressure of potassium) as a function of temperature is presented in Figure 3. $K_{0.97}B_6$ exhibits activated conductivity above 170 K (with activation energy 26 meV) and temperature-independent conductivity below 170 K. The thermoelectric power measurements for $K_{0.97}B_6$ using sintered samples under saturation vapor pressure of potassium show that the Seebeck coefficient is positive (inset of Figure 3). The thermoelectric power is consistent with the view that $KB_6$ is a metal with hole-type carriers, while the resistance measurements suggest a need to consider the occurrence of electron localization in $KB_6$. However, it should be noted that transport properties of powder samples are strongly affected by electron transport between grain boundaries, which is sensitive to sintering. Thus, measurements of other physical properties are necessary to understand the nature of electrons in the partially empty bands of $KB_6$.

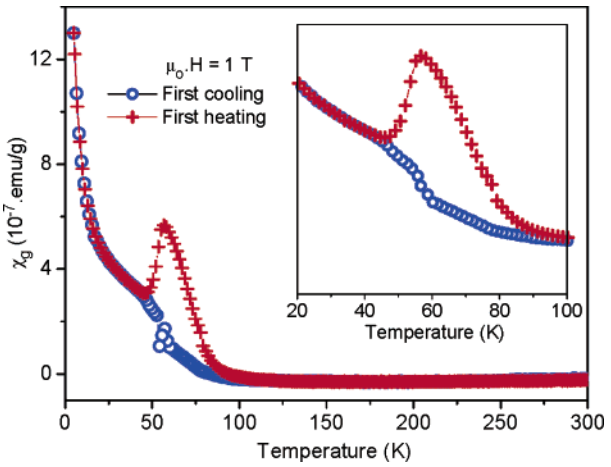


**Figure 4.** Thermal variation of the magnetic susceptibility of $K_{0.97}B_6$ measured for the first cooling and first heating cycle with cooling/heating rate $\upsilon = 10$ K/min. The inset shows the corresponding results determined with a slow cooling/heating rate (i.e., $\upsilon = 1$ K/min for the 4.2−100 K region and 10 K/min for the 100−300 K region) (taken from Figure 1 of ref 28).

**3.2. Magnetic Susceptibility.** The magnetic susceptibility data of $K_{0.97}B_6$ were reported in our previous study.[28] Thus, in this section, we briefly summarize the essential findings of the magnetic susceptibility data. Figure 4 shows the magnetic susceptibility curves of $K_{0.97}B_6$, measured while cooling the sample from room temperature to 4.2 K (the first cooling) and subsequently heating from 4.2 K to room temperature (the first heating) under $\mu_0 H = 1$ T with cooling/heating rate $\upsilon = 10$ K/min. $K_{0.97}B_6$ appears practically diamagnetic above 100 K, and the susceptibility for the first heating cycle is different from that for the first warming cycle. The slow cooling/heating rate does not radically alter the nature of the susceptibility curves (see the inset of Figure 4). When the sample was quickly cooled to 57 K under $\mu_0 H = 1$ T at the end of the first heating at room temperature and the susceptibility is measured as a function of time while staying at 57 K (under $\mu_0 H = 1$ T), then the susceptibility increases gradually as a function of time almost reaching the susceptibility peak value in 50 min (not shown). Figure 5 shows that the second cooling and the second heating cycles reproduce the susceptibility hysteresis found in the first cooling and the first heating cycles ($\mu_0 H = 1$ T and $\upsilon = 10$ K/min). In our third cooling cycle, we quenched the sample from 100 to 40 K under $\mu_0 H = 1$ T and then measured the susceptibility for the third heating cycle. The third heating curve has a lower susceptibility than does the second heating curve at 40 K and produces a susceptibility peak with a slightly lower intensity compared with that of the second heating cycle. The fourth cooling curve from 100 to 40 K with $\upsilon = 10$ K/min is superimposed on the second cooling curve. All these observations indicate that $K_{0.97}B_6$ undergoes a slow relaxation process below 100 K.

**3.3. EPR Measurements. A. X-Band (9.5 GHz) EPR.** The EPR data for $K_{0.97}B_6$ measured using conventional continuous wave X-band EPR were also reported in our previous study.[28] Thus, the essential findings of these EPR

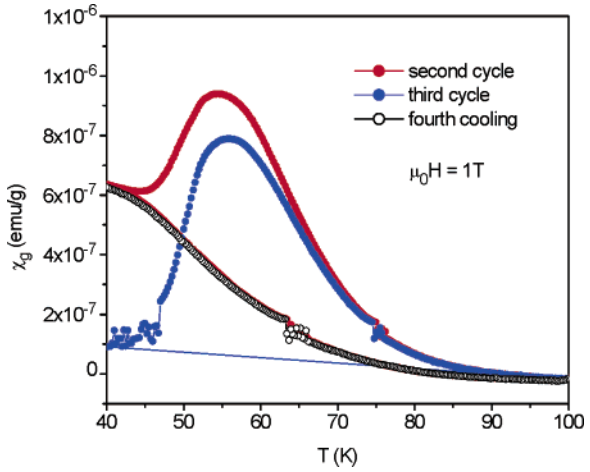


**Figure 5.** Magnetic susceptibility of $K_{0.97}B_6$ measured for the second cooling/heating cycles, for the quenching/third heating cycles, and for the fourth heating cycle.

data are briefly summarized. The powder sample of $K_{0.97}B_6$ was first cooled to 4.2 K in the absence of magnetic field, and a set of EPR spectra was taken while heating the sample to room temperature (RT). After that, the sample was cooled back to 4.2 K. The effective heating/cooling rate for the EPR studies was less than 1/10 that utilized in magnetic susceptibility measurements. Typically, EPR spectra were taken at microwave frequency of 9.465 GHz, incident microwave power = 0.2 mW, center field = 3500 G, and sweep width = 7000 G, and were digitized to 1024 points. At 4.2 K, a narrow signal is superimposed on a broad signal (the peak-to-peak line widths $\Delta H_{pp}$ of ~26.4 and ~315 G, respectively) (see Figure 2 of ref 28). The narrow signal is hidden under the broad signal at RT and becomes clearly visible below 100 K. The $\Delta H_{pp}$ of the broad signal is practically temperature independent. The EPR susceptibility (obtained by double integration of the EPR signal) for the heating and cooling cycles show a strong hysteresis below 100 K, as do the magnetic susceptibility curves (see Figure 3 of ref 28). However, the EPR susceptibility for the cooling cycle differs from the magnetic susceptibility of the first cooling cycle in that the former exhibits a prominent susceptibility peak around 52 K, while the latter shows a small kink at 53−58 K.

Thus, our X-band EPR results showed that $K_{0.97}B_6$ has localized electrons above 100 K and that there exist two kinds of environments for the unpaired spins, one responsible for the broad EPR signal and the other for the narrow one. To understand what kind of slow relaxation process the localized electrons of $K_{0.97}B_6$ undergo, we estimated what fraction of a spin/FU is responsible for the narrow and broad EPR peaks ($f_N$ and $f_B$, respectively). The comparison of the areas of the integrated narrow and broad EPR peaks showed that $f_N$ is a very small fraction of $f_B$, i.e., $f_N/f_B = 2 \times 10^{-3}$ at 4.2 K, $5 \times 10^{-4}$ at 20 K, and $3 \times 10^{-4}$ at 30 K (for the estimation of the RT value of $f_N/f_B$, see below). The narrow EPR signal (sweep width = 130 G) clearly shows evidence for a hyperfine structure (of at least 10 lines) centered at $g = 2.0025$ (inset of Figure 2 in ref 28). To estimate the $f_B$ value for the broad EPR peak, we compared the double integral corresponding to the area of the broad peak of $K_{0.97}B_6$ with that of the EPR peak of $CuSO_4 \cdot 5H_2O$, which has one unpaired spin/FU, measured under the same experimental conditions. In the absence of the saturation effects, the double integral of the first derivative EPR signal, $A$, depends on the number of spins/FU, $f$, the number of the functional units in the sample, $N$, and the microwave power, $P$, as $A \propto fN\sqrt{P}$. To ensure the absence of temperature-dependent saturation effects on EPR signals, EPR spectra of $K_{0.97}B_6$ and $CuSO_4 \cdot 5H_2O$ at a given temperature were measured at two different incident microwave powers of $P = 0.200$ and 0.795 mW. From these measurements, the $f_B$ values are estimated to be in the range of $10^{-3}-10^{-2}$ spin/FU (i.e., $8 \times 10^{-4}$ spin/FU at 4.2 K, $9 \times 10^{-3}$ spin/FU at 60 and 100 K, and $3 \times 10^{-2}$ spin/FU at 291 K). Therefore, the average size of a "domain" (to be referred to as a spin bag) leading to the broad EPR signal would be of the order of 1250 $B_6$ octahedra at 4.2 K to 33 $B_6$ octahedra at 291 K. If such a spin bag is approximated by a cube with side length $L = Na$, where $a$ is the unit cell parameter (i.e., 0.42 nm) and $N$ is the number of $B_6$ octahedra forming the side of the cube, then $N$ ranges from ~3.2 at 291 K to ~11 at 4.2 K, so that $L$ ranges from ~1.3 nm at 291 K to ~4.5 nm at 4.2 K. Our SEM measurements of powder $K_{0.97}B_6$ samples (Figure 2) show tiny cubic single crystals with side length smaller than 700 nm. Since $KB_6$ is an odd number of valence electrons/FU (i.e., 19), there can be in principle one spin/FU. From this localized viewpoint, most spins are paired up and only a small number of spins are left over in $KB_6$. Namely, on average, every 33 FU's have one spin responsible for the broad EPR peak at 291 K and every 1250 FU's do at 4.2 K.

**B. Effect of Microwave Frequency on EPR Signal and Its Implication.** To further characterize the nature of EPR signals of $K_{0.97}B_6$ we have carried EPR measurements at several different EPR frequencies, i.e., 1.38, 8.8−9.5, 35, 94, and 186 GHz. Due to the broad range of EPR frequencies, it was necessary to utilize different EPR spectrometers. This required the use of sample tubes of different sizes. The powder sample was flame-sealed in a short (ca. 15 mm long) quartz tube of 3 mm inner diameter and 4 mm outer diameter for measurements at L-band (1.38 GHz) and X-band (9.8−9.5 GHz) and also for measurements at 94 and 186 GHz using a quasi-optical EPR spectrometer at the National High Magnetic Field Laboratory (Tallahassee, FL). Two other EPR spectrometers utilized in our study, a Varian Century Series Q-band (35 GHz) and a W-band (95 GHz) spectrometer built at the Illinois EPR Research Center, were equipped with cylindrical $TE_{011-012}$-type resonators that cannot use sample tubes with outer diameter larger than 0.95 mm (W-band) and 2.0 mm (Q-band). For these Q- and W-band measurements, the sample was flame-sealed inside thin-wall 0.7 × 0.87 mm quartz capillaries (VitroCom, Mountain Lakes, NJ).

Figure 6 shows an X-band (9.5 GHz) EPR spectrum obtained at RT. Although the contribution of a narrower signal is hard to see in this spectrum, least-squares simulations reveal its presence; the spectrum is well modeled as a superposition of a broad Lorentzian shape with a less intense and much narrower signal. The narrow signal at this temperature and resolution is also well modeled as a

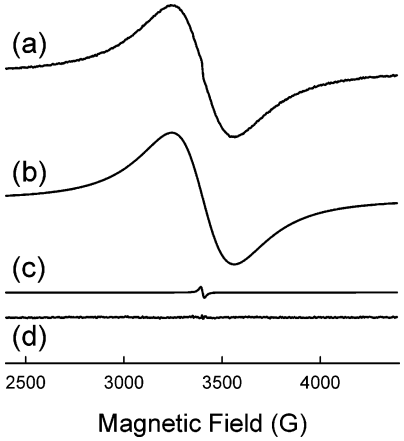


**Figure 6.** Simulation of the EPR spectrum of $K_{0.97}B_6$ obtained at room temperature using 9.5 GHz: (a) the experimental spectrum; (b) the calculated spectrum for the broad peak ($\Delta H_{pp} = 318.0$ G); (c) the calculated spectrum of the narrow peak ($\Delta H_{pp} = 18.0$ G); (d) the difference between the experimental and the calculated spectra.

Lorentzian function. The residual of least-squares simulations (i.e., the difference between experimental and simulated spectra), shown in Figure 6, demonstrates that this model fits the experiment exceptionally well. The simulations for the peak-to-peak line widths show that $\Delta H_{pp} = 318.0 \pm 0.5$ G for the broad component and $\Delta H_{pp} = 18.0 \pm 0.5$ G for the narrow component. From these simulations we estimate that the $f_N/f_B$ value is estimated to be $3 \times 10^{-4}$ at room temperature, which is consistent with the corresponding values estimated at 4.2, 20 and 30 K.

The shape of the broad EPR signal is consistent with an exchange-narrowed spectrum, which is Lorentzian in the center and Gaussian in the wings. The frequency dependence of an exchange-narrowed spectrum depends on the effective dimensionality of the spin system. For a 3D system, $\Delta H_{pp}$ is related to the EPR frequency $\omega_0$ as follows:[29]

$$\Delta H_{pp} = \frac{H_d^2}{H_e}\left(1 + \frac{5}{3}e^{-0.5(\omega_0/\omega_e)^2} + \frac{2}{3}e^{-2(\omega_0/\omega_e)^2}\right) \qquad (1)$$

Here $H_d$ is the dipolar field, $H_e$ is the exchange field, and $\omega_e = \gamma H_e$ is the exchange frequency. This expression predicts that as the frequency $\omega_0$ of EPR experiments is increased, i.e., as $(\omega_0/\omega_e) \rightarrow \infty$, the line width decreases until it reaches the limiting value $\Delta H_{pp} = H_d^2/H_e$. Other terms such as the *g*-factor anisotropy and the distribution of *g*-factors (i.e., the *g*-strain) may also contribute so that $\Delta H_{pp}$ is modified as

$$\Delta H_{pp} = \frac{H_d^2}{H_e}\left(1 + \frac{5}{3}e^{-0.5(\omega_0/\omega_e)^2} + \frac{2}{3}e^{-2(\omega_0/\omega_e)^2}\right) + X\omega_0 + X'\omega_0^2 + C' \qquad (2)$$

where $X\omega_0$ describes line width broadening due to the *g*-strain and EPR instrumentation, $X'\omega_0^2$ expresses broadening due to the difference in *g*-factors of the magnetically nonequivalent sites in the presence of exchange, and $C'$ is the residual line width.[30,31] Equation 2 predicts that the EPR line width should eventually increase with increasing $\omega_0$ at very high EPR frequencies.

The EPR spectra of $K_{0.97}B_6$ measured by different $\omega_0$ from 1.38 to 184 GHz are summarized in Figure 7. The left-hand side of the figure shows room-temperature spectra at 1.38, 9.52, 92.8, and 184 GHz. Least-squares simulations shown on the right-hand side of the figure were corrected for a baseline drift and a dispersion contribution. (The latter are responsible for the asymmetric line shape of the 184 GHz spectrum in Figure 7d.) Due to the low signal-to-noise ratio of the latter spectrum, it was unchanged over more than 2 orders of magnitude in the EPR frequency; our least-squares simulations show that the variation of $\Delta H_{pp}$ is within $\pm 2\%$. It should be noted that the shape of the EPR signal remains the same even at L-band (1.38 GHz). When the magnetic field was swept over the maximum allowed range from 41 to 981 G at this fixed-frequency experiment, the center of the spectrum was observed at ca. 491 G. Thus, while the magnitude of magnetic field increases by a factor of about 2 from the lower field minimum of the first-derivative EPR signal to the upper field maximum, the shape of the EPR signal remains Lorentzian. Therefore, at RT, the EPR signal has no magnetic field dependence down to a few hundred gauss. The line width and the line shape of all $K_{0.97}B_6$ samples studied remains essentially the same over a broad range of EPR resonance conditions spreading from 1.38 to 186 GHz (corresponding magnetic fields from ca. 490 to 66 100 G). The absence of any dependence of EPR signal in such a broad range of resonance frequencies is rarely observed. In view of the Anderson−Weiss theory[30] discussed above, it is concluded that the exchange frequency is much lower than the lowest frequency of the EPR experiment (i.e., $\omega_e \ll \omega_0 = 1.38$ GHz) and that the *g*-anisotropy is too small to contribute to any additional line broadening even at 184 GHz.

One possible mechanism for such a frequency/field independent line width could be a pure dipolar (through-space) spin−spin interaction.[31] There are several theoretical treatments of dipolar spin−spin interactions in solids. In the past the Van Vleck moments method and the statistical line shape theory have been used successfully to analyze static dipolar broadening of EPR lines in solids.[32,33] Although the moments method is straightforward to employ, an accurate calculation of the second moments from the EPR data is not an easy task and is subject to relatively large errors originating from the sloping baselines and the noise at the far wings of the spectra. Thus, a line shape analysis is more reliable. There are some modifications of the Van Vleck moments method that could also be used to derive the shape of dipolar broadening. In the absence of exchange and hyperfine interactions, the resonance shape is Gaussian if more than 10% of the lattice sites are occupied by the paramagnetic ions and is approximated by a Lorentzian when the occupancy falls below 10%.[34] Under the latter conditions,

(29) Anderson, P. W.; Weiss, P. R. *Rev. Mod. Phys.* **1953**, *25*, 1.
(30) Cage, B.; Cevc, P.; Blinc, R.; Brunel, L.-C.; Dalal, N. S. *J. Magn. Reson.* **1998**, *135*, 178.
(31) Smirnov, A. I.; Sen, S. *J. Chem. Phys.* **2001**, *115*, 7650.
(32) Van Vleck, H. *Phys. Rev.* **1948**, *74*, 1168.
(33) Kubo, R.; Tomita, K. *J. Phys. Soc. Jpn.* **1954**, *9*, 888.
(34) Kittel, C.; Abrahams, E. *Phys. Rev.* **1953**, *90*, 238.

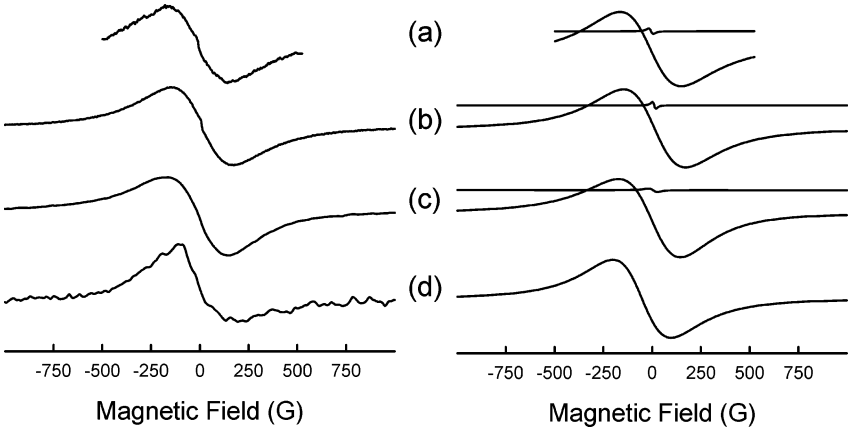


**Figure 7.** Room-temperature EPR spectra of $K_{0.97}B_6$ measured at various EPR frequencies $\omega_0$: (a) $\omega_0 = 1.38$ GHz; (b) $\omega_0 = 9.52$ GHz; (c) $\omega_0 = 92.8$ GHz; (d) $\omega_0 = 184$ GHz. The left-hand side shows the experimental spectra, and the right-hand side the least-squares simulations.

predominantly a Lorentzian line shape is also predicted from calculations based on statistical methods. For example, for solids of spin-1/2 sites, $\Delta H_{pp}$ is related to the spin concentration $C$ as follows:[35]

$$\Delta H_{pp} = 2\left(\frac{2\pi}{3}\right)^3 g\beta C \qquad (3)$$

Here $g$ is the electron $g$-factor and $\beta$ is the Bohr magneton. If we assume a uniform distribution of spin-1/2 sites in $KB_6$, then the resulting EPR signal should be well modeled by a Lorentzian function and eq 3 can be used to estimate the interspin distance. If the isotropic spin arrangement is assumed, the $C$ value obtained from eq 3 using $\Delta H_{pp} = 310$ G shows that the side length of a cube containing one unpaired spin is approximately 1.0 nm. The latter value may be an underestimate because this estimation is based on the assumption that the width of the broad EPR signal arises solely from dipolar origin, but there can be other contributions to the width (e.g., unresolved hyperfine interactions).

The average distance of ~1.0 nm between adjacent spins deduced from the $\Delta H_{pp}$ value of the broad peak is consistent with the value of ~1.3 nm estimated from the peak area at 291 K in the previous section. However, it is not consistent with the value of ~11 nm estimated from the peak area at 4.2 K. This discrepancy can be resolved if there exist structural units responsible for the broad EPR peak in $KB_6$, in which the average distance between spins is approximately 1.0 nm and if the concentration of these structural units decrease with decreasing temperature from RT. An implication of the latter observation will be discussed in section 6.

**3.4. Solid-State Magic Angle Spinning (MAS) NMR. A. $^{39}$K MAS NMR.** The $^{39}$K MAS NMR spectrum of $K_{0.97}B_6$ is shown in Figure 8, which also shows the spectrum of solid KCl measured under identical conditions (11.75 T magnet, 23.3 MHz, single short pulse, 5 kHz spinning), where the spectra are referenced to that of a 1 M aqueous solution of KCl (0 ppm). $^{39}$K is not commonly used for NMR, because of its very low magnetogyric factor. With respect to the $K^+$ solution, solid KCl resonates at 49 ppm and solid KBr at 55 ppm (not shown). Thus, the range of the $^{39}$K chemical shift is rather wide for very similar compounds. This is due most likely to a large polarizability of the electron cloud around K, whose screening effect opposing the applied field can be significantly affected by the surrounding atoms. In addition, we carried out measurements to record the $^{39}$K MAS NMR signal of $K_8Si_{46}$ and $K_{0.67}CoO_2$, both of which are materials with metallic conductivity with an expected participation of K to the density of states (DOS) at the Fermi level. Indeed, in these two compounds, the $^{39}$K NMR signal could not be observed, due to too strong hyperfine interactions. Consequently, the NMR peak of $K_{0.97}B_6$ observed at 150 ppm does not show a significant hyperfine shift caused either by electron spins or by delocalized electrons present on the K nucleus. This suggests that potassium in $KB_6$ exists as $K^+$. Indeed, electronic band structure calculations for $KB_6$ show a very small contribution of K at the Fermi level (section 5), in agreement with the small shift of the NMR line.

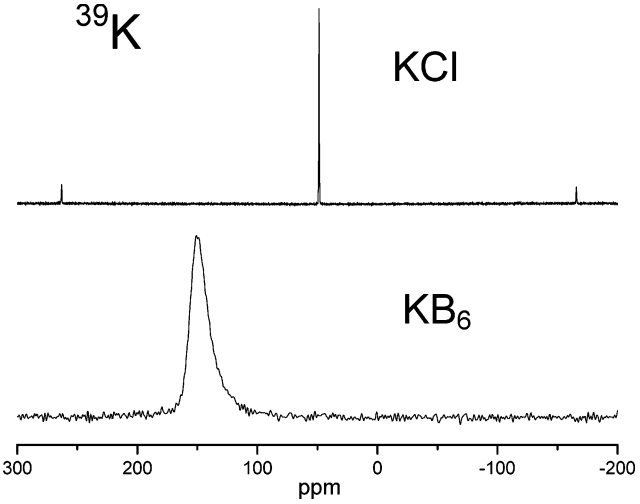


**Figure 8.** $^{39}$K MAS NMR spectra of (bottom) $K_{0.97}B_6$ and (top) solid KCl (11.75 T magnet, 23.3 MHz, single short pulse, 5 kHz spinning; 0 ppm reference: 1 M aqueous solution of KCl).

The width and shape of the $^{39}$K MAS NMR signal are quite different from those of solid KCl. Since $^{39}$K is a spin-3/2 nucleus, one might consider the line shape to be affected by second-order quadrupolar effects. However, the line shape observed is not characteristic of such effects. The width of

(35) Grant, W. J. C.; Strandberg, M. W. P. *Phys. Rev.* **1964**, *135*, A715.

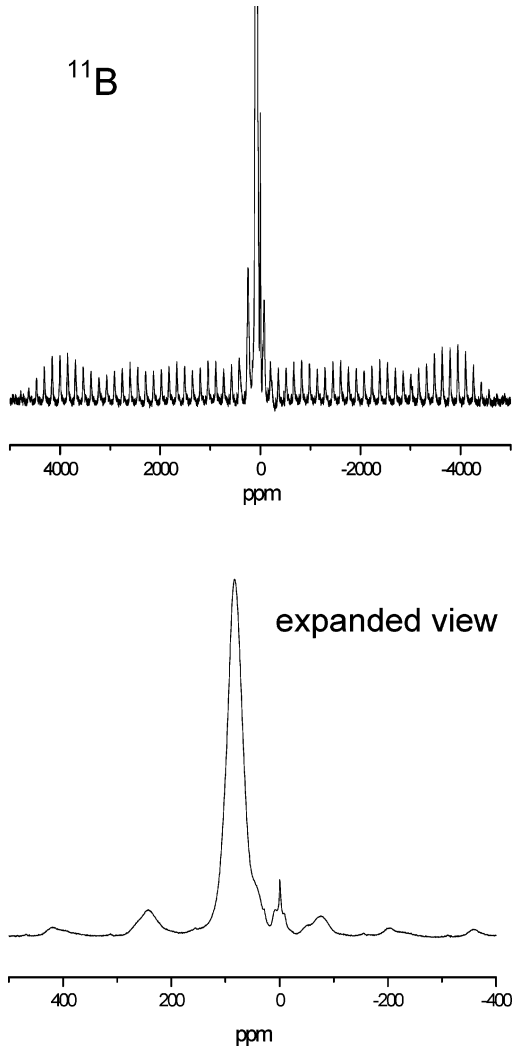


**Figure 9.** $^{11}$B MAS NMR spectrum of $K_{0.97}B_6$ (7 T, 96.3 MHz, short single pulse, 15 kHz spinning; 0 ppm reference: tetrahedral boron of $Na_2B_4O_7$): (top) large-scale view; (bottom) zoomed-in view of the central line.

the line could be due to residual dipolar interactions with electron spins or conducting electrons, not fully averaged out by MAS. However, the structure of the line suggests a distribution of signals with various intensities and hence that of locally different K environments. The latter would arise from the K nonstoichiometry, since it gives rise to K atoms with different arrangements of surrounding K atoms and vacant K positions, as confirmed by the recording of $^{39}$K MAS NMR spectra for $KB_6$ samples with slightly different actual stoichiometries (not shown).

**B. $^{11}$B MAS NMR.** The single pulse $^{11}$B MAS NMR spectrum (7 T, 96.3 MHz, short single pulse, 15 kHz spinning; 0 ppm reference, tetrahedral boron of $Na_2B_4O_7$) for $K_{0.97}B_6$ is shown in Figure 9, with a zoomed view of the central line. $^{11}$B is also a spin-3/2 nucleus, so that the three NMR transitions (3/2 to 1/2; 1/2 to $-1/2$; $-1/2$ to $-3/2$) do not occur at the same frequency, as long as the electric field gradient (EFG) around B deviates from the perfect spherical symmetry (the first-order quadrupolar effect). This leads to the very large number of spinning sidebands observed in the spectra. The central transition ($-1/2$ to 1/2) is responsible for the most intense signal at the center. All other signals are spinning sidebands of the satellite transitions, which are spread over a very wide frequency range. In addition, despite its weak quadrupolar moment, $^{11}$B easily exhibits second-order quadrupolar effects due to the covalency of its bonds with the surrounding atoms. Namely, the electron cloud around $^{11}$B has the symmetry of the bond arrangement, which leads to nonspherical EFG's and hence the classical second-order line shape of the central line with two bumps as can be seen, for example, for 3-fold-coordinated boron in borates. Such a signal is clearly observed in the spectrum of $K_{0.97}B_6$ (at $+10/-10$ ppm). In addition, a sharp signal at 0 ppm is also observed, typical of a tetrahedrally coordinated boron, with no second-order quadrupolar line shape showing a close-to-spherically symmetrical environment. The $+10/-10$ ppm and the 0 ppm signals are assigned respectively to triangular and tetrahedral borons belonging to some borate impurities probably present on the surface of the $KB_6$ sample.

The central line for $^{11}$B in $K_{0.97}B_6$ (84 ppm) does not exhibit second-order quadrupolar characteristics. However, this line is both rather broad (with a shoulder at 50 ppm) and quite shifted. The shift is due most probably to the contact contribution of the hyperfine interactions. In principle, this shift is due either to the presence of some density of electron spins on the boron nuclei (Fermi contact) or to the participation of an s orbital of boron to the Fermi level so that the nucleus experiences the Pauli paramagnetism of the conducting electrons (Knight shift). The width of the signal might partly result from residual dipolar interactions with electron spins or with other $^{11}$B nuclei (homonuclear), despite MAS. However, it is rather assigned, as well as the shoulder, to distributions of boron environments. This was confirmed by the observation of $^{11}$B MAS NMR spectra for a series of $KB_6$ samples with different actual stoichiometries (not shown).

To help interpret what the NMR signal of $KB_6$ implies, we have also carried out $^{11}$B MAS NMR measurements of $CaB_6$ and $LaB_6$. $CaB_6$ is either a small gap semiconductor or a semimetal, while $LaB_6$ is a good metal. For $CaB_6$ a small shift (15 ppm) and a large relaxation time $T_1$ (120s) are observed. This is consistent with a very small amount of electron spins, expected for a semimetal or a very small gap semiconductor. For $LaB_6$, which is a good metallic conductor, the chemical shift is very small (2 ppm) and the relaxation time is very short (5 ms). These observations are consistent with the fact that the electrons at the Fermi level are in the La 5d states. For $K_{0.97}B_6$ the shift is relatively large (84 ppm) and the relaxation time is relatively short (50 ms) by comparison with that of $CaB_6$. These findings indicate either the presence of localized electron spins in $K_{0.97}B_6$, with some spin density at the B nucleus sites (Fermi contact shift), or the presence of conducting electrons, with some electron density present in an s orbital of boron (positive Knight shift). As shown in section 5, the B 2s contribution at the Fermi level is negligible. In a metallic picture, because the Fermi level lies in p orbitals of boron, one would expect a negative Knight shift due to the

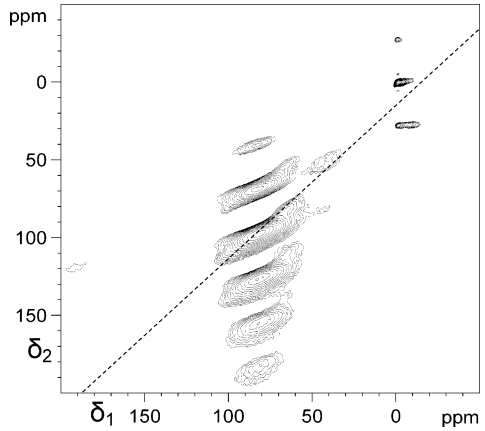


**Figure 10.** $^{11}$B triple quantum MAS NMR spectrum of $K_{0.97}B_6$ (7 T, 96.3 MHz, 15 kHz spinning; 0 ppm reference: tetrahedral boron of $Na_2B_4O_7$; horizontal axis, $\delta_2 = \delta_{CS} + \delta_{QIS}$; vertical axis, $\delta_1 = \delta_{CS} - (10/17)\delta_{QIS}$ (see text)). The chemical shift distribution line is shown by the dotted line.

polarization of the electrons in the s orbital by the conduction electrons in the p orbital. One can therefore conclude that the positive shift observed by NMR is a Fermi contact shift, showing the presence of localized electron spins with a weak transfer on the potassium s orbital, which is consistent with the magnetic susceptibility and EPR measurements.

To further understand the $^{11}$B NMR line shape, we have carried out $^{11}$B 3Q-MAS experiments (Figure 10). In this 2D experiment, one allows a triple quantum coherence (3/2 to −3/2 transition) to evolve and then converts it into an observable coherence, thus creating the corresponding free induction decay in the second dimension. In the 2D map, the horizontal axis corresponds to the usual MAS dimension, where the signals position $\delta_2$ is the sum of the chemical (or Fermi contact) shift $\delta_{CS}$ and the second-order quadrupolar induced shift $\delta_{QIS}$ (i.e., $\delta_2 = \delta_{CS} + \delta_{QIS}$), while the vertical axis corresponds to the so-called isotropic dimension, where the signals position $\delta_1$ is a different linear combination of the two kinds of shifts [i.e., $\delta_1 = \delta_{CS} - (10/17)\delta_{QIS}$]. Therefore, the line with slope 1 (i.e., the chemical shift distribution line) contains signals of identical second-order quadrupolar induced shifts, i.e., where only the chemical (or Fermi contact) shift changes. In the case of $KB_6$, the result presented in Figure 10 shows two signals corresponding to the main signal and the shoulder observed in the 1D experiment of Figure 9, repeated vertically due to MAS (one can also observe the signals of the borate impurity at 0 ppm). It appears that the two spots are elongated and aligned in a direction close to the chemical shift distribution line. This suggests that the corresponding boron atoms differ essentially in their shift (which in the present case is a Fermi contact one) rather than in the symmetry of the electrical field gradient they experience (which generates the second-order quadrupolar effect). Thus, it is likely that the two types of boron atoms corresponding to the two NMR signals differ in their electronic state, i.e., in the number of electrons that have been transferred to them by the surrounding K ions. The two types of signals would therefore correspond to different zones in the sample where the extents of K atom vacancies are substantially different.

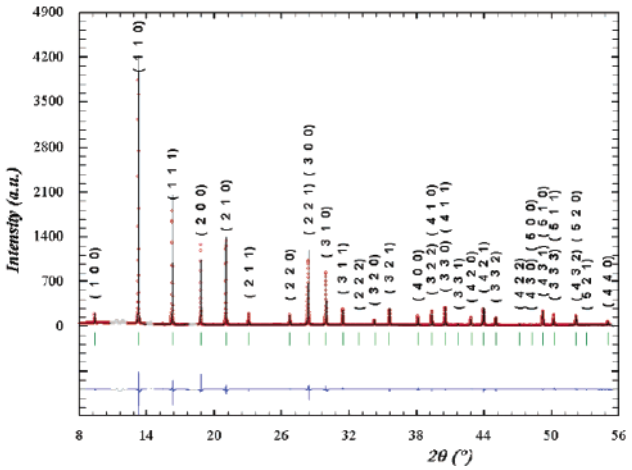


**Figure 11.** Observed versus calculated powder diffraction pattern of $KB_6$ at 60 K. Excluded regions contain small peaks of an impurity phase.

**Table 2.** Conditions of the X-ray Diffraction Data Collection for $KB_6$ at Different Temperatures

| temp (K) | 2$\theta$(initial) (deg) | av step (deg) | 2$\theta$(final) (deg) |
|---|---|---|---|
| 25.00 | 4.0180 | 0.0082 | 55.4812 |
| 35.00 | 12.0294 | 0.0082 | 22.2876 |
| 45.00 | 12.0310 | 0.0082 | 22.2810 |
| 48.00 | 8.0278 | 0.0082 | 30.4794 |
| 55.00 | 8.0278 | 0.0082 | 30.4794 |
| 60.00 | 4.2124 | 0.0062 | 55.4926 |
| 75.00 | 12.0212 | 0.0082 | 21.9760 |
| 100.00 | 12.0212 | 0.0082 | 21.9760 |
| 150.00 | 12.0212 | 0.0082 | 21.9842 |
| 200.00 | 12.0212 | 0.0082 | 21.9760 |
| 250.00 | 12.0294 | 0.0082 | 20.4836 |
| 300.00 | 5.0266 | 0.0082 | 45.7970 |

## 4. Crystal Structure of $KB_6$ as a Function of Temperature

The high-resolution X-ray synchrotron powder diffraction experiment on $KB_6$ was performed on the Swiss−Norwegian Beam Line BM1 at ESRF. A capillary of 0.7 mm diameter was used as sample holder. The 2-circle diffractometer has a set of six detector/analyzers mounted in the 2$\theta$ circle, which allows one to collect six complete patterns simultaneously, with an offset in 2$\theta$. The angular offset between the detectors is close to 1.1°. The analyzers are Si-111 crystals in front of each detector (Na−I scintillation counter), resulting in an intrinsic resolution (fwhm) of approximately 0.01° at a wavelength of 1 Å. We have worked at a wavelength of 0.689 433(3) Å. The capillary with the sample was mounted in a spinner inside a He cryostat, and we worked at temperatures between 25 and 300 K. We have performed a set of scans, of different 2$\theta$ ranges, at the temperatures collected in Table 2.

The powder diffraction patterns show the presence of a small quantity of an impurity phase (probably $KBO_3$ in agreement with the $^{11}$B NMR observation), which does not interfere with the main $KB_6$ cubic phase. We have performed Rietveld refinements of all the data and fixed the zero shift to that found at 60 K (the highest quality data) to obtain reliable values of the cell parameter (Figure 11). The most complete diffraction patterns correspond to those collected at 25 K, 60 K, and RT. The other patterns are limited to a

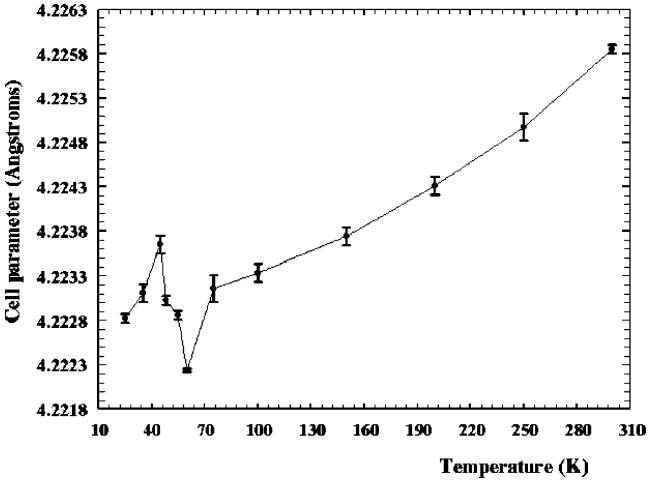


**Figure 12.** Cell parameter of $KB_6$ as a function of temperature.

**Table 3.** B−B and K−B Distances (in Å) of $KB_6$ at Three Selected Temperatures

| temp (K) | K−B | BB2 | BB1 |
|---|---|---|---|
| 300.00 | 3.1023(9) | 1.8033(19) | 1.6744(27) |
| 60.00 | 3.1006(5) | 1.7970(11) | 1.6796(15) |
| 25.00 | 3.1012(7) | 1.7961(15) | 1.6815(21) |

few reflections (only 3 in the diffraction pattern at 250 K). The refinement gives typical *R*-Bragg factors as 2.2% (RT), 2.7% (60 and 25 K), and, the worst, 4.7% (250 K, only three reflections). The structure of $KB_6$ is maintained throughout the whole temperature range (space group is *Pm*3*m*) with the K atom in Wyckoff position 1b (1/2, 1/2, 1/2) and the B atom in Wyckoff position 6e ($x$, 0, 0) ($x \approx 0.3018$). The sample is slightly under stoichiometric in K. The temperature dependence of the structural parameters of $KB_6$ is summarized in Table 1.

The Bragg reflections are broadened with respect to the instrumental resolution function. The isotropic size and strain Lorentzian-like parameters were refined. The average crystallite size oscillates between 450 nm (between RT and 75 K) and 480 nm (at 60 K and below), which are consistent with the particle sizes estimated from the SEM picture of Figure 2. The maximum strain is around $6.6 \times 10^{-4}$ (above 75 K) and $7.0 \times 10^{-4}$ (below 60 K). There is a slight broadening below 70 K, which may be related to changes in the cell parameter and magnetostriction effects. The changes in cell and size/strain parameters are quite small.

The variation of the cell parameter as a function of temperature is shown in Figure 12. Between RT and ~70 K the dependence of the cell parameter on temperature is usual, i.e., a gradual decrease in the cell parameter with decreasing temperature. Below ~70 K, however, the cell parameter shows an unusual temperature dependence. The variations of the B−B and K−B distances as a function of temperature are summarized in Table 3. As the temperature is lowered from RT to 25 K, the $B_6$ octahedron contracts gradually (i.e., BB2 decreases gradually). However, the K−B and the inter-octahedron BB1 distances exhibit a minimum around 60 K, as does the cell parameter. These findings strongly support that the hysteresis in the magnetic susceptibility and EPR susceptibility observed below 100 K is a bulk phenomenon.

**Table 4.** Exponents $\zeta_i$ and Valence Shell Ionization Potentials $H_{ii}$ of Slater-Type Orbitals $\chi_i$ Used for Extended Hückel Tight-Binding Calculations[a]

| atom | $\chi_i$ | $H_{ii}$ (eV) | $\zeta_i$ | $c_1$ [b] | $\zeta_i$ | $c_2$ [b] |
|---|---|---|---|---|---|---|
| B | 2s | −13.4 | 1.413 | 0.8710 | 0.8760 | 0.1852 |
| B | 2p | −8.40 | 2.217 | 0.2153 | 1.1060 | 0.8405 |
| K | 4s | −4.00 | 1.205 | 1.0000 | | |
| K | 4p | −2.76 | 1.100 | 1.0000 | | |

[a] $H_{ii}$'s are the diagonal matrix elements $\langle\chi_i|H^{\text{eff}}|\chi_i\rangle$, where $H^{\text{eff}}$ is the effective Hamiltonian. In our calculations of the off-diagonal matrix elements $H^{\text{eff}} = \langle\chi_i|H^{\text{eff}}|\chi_j\rangle$, the weighted formula was used.[41,42] [b] Coefficients used in the double-$\zeta$ Slater-type orbital expansion.

## 5. Electronic Band Structure of $KB_6$

The electronic structure of the normal metallic state of $KB_6$ was calculated within the framework of the density functional theory (DFT) using the augmented plane wave plus local orbitals (APW + lo) method, implemented in the WIEN2k code.[36] For the exchange-correlation potential the generalized gradient approximation (GGA)[37] was employed. APW + lo calculations were carried out using the experimental crystal structure, muffin-tin radii of 2.0 and 1.63 au for K and B, respectively, and cutoff parameters $G_{\max} = 14$ and $RK_{\max} = 7.0$. A 56 k-points mesh was used for integrations over the irreducible wedge of the cubic Brillouin zone. We also calculated the electronic structures of $KB_6$ with the extended Hückel tight-binding (EHTB)[38,39] method using the atomic parameters listed in Table 4, where the B 2s/2p orbitals are represented by double-$\zeta$ Slater type orbitals and the K 4s/4p orbitals by single-$\zeta$ Slater type orbitals.[40] After verifying that the EHTB method reproduces the electronic structures obtained from the first principles calculations, it was used to analyze the nature of the band structures around the Fermi level on the basis of orbital interactions.

As discussed in section 3, the physical properties of $KB_6$ indicate that $KB_6$ is not a normal metal but it has localized electrons. A system with partially filled bands can be a metal but is subject to electron localization induced by electron−electron repulsion (Mott−Hubbard localization),[23] by random potential (Anderson localization) associated with lattice defects,[24] or by electron−phonon coupling as found for polaronic states.[25] Electron localization causes the extent of the electron wave function to have a finite length. If this localization length is short, the electrons are strongly localized so that the system behaves as an insulator, its charge transport occurs through hopping, and its resistivity increases strongly with decreasing the temperature. In a weakly disordered system, however, the localization length can be long and even longer than the inelastic scattering length. In

(36) Blaha, P.; Schwarz, K.; Madsen, G. K. H.; Kvasnicka, D.; Luitz, J. *An augmented plane wave plus local orbitals program for calculating crystal properties*; University of Technology: Vienna, Austria, 2001; ISBN 3-9501031-1-2; WIEN2k, http://www.wien2k.at.
(37) Perdew, J. P.; Burke, S.; Ernzerhof, M. *Phys. Rev. Lett.* **1996**, *77*, 3865.
(38) Whangbo, M.-H.; Hoffmann, R. *J. Am. Chem. Soc.* **1978**, *100*, 6093.
(39) Our calculations were carried out by employing the *CAESAR* program package (Ren, J.; Liang, W.; Whangbo, M.-H. *Crystal and Electronic Structure Analysis Using CAESAR*; North Carolina State University: Raleigh, NC, 1998; http://chmwva.chem.ncsu.edu).
(40) Clementi, E.; Roetti, C. *At. Data Nucl. Data Tables* **1974**, *14*, 177.

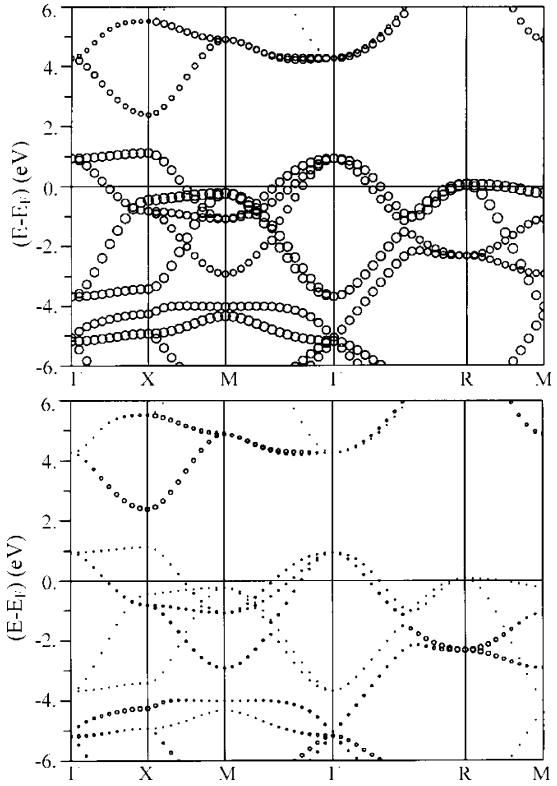


**Figure 13.** Fat band representations of the dispersion relations of the electronic band structure of $KB_6$ calculated by the APW + lo method (top: boron character. bottom: potassium character). The size of the spots for K has been magnified by 6 to account for the stoichiometry and to emphasize the almost pure boron character of bands in this energy range. Γ = (0, 0, 0), $X$ = ($a$*/2, 0, 0), $M$ = ($a$*/2, $b$*/2, 0), and $R$ = ($a$*/2, $b$*/2, $c$*/2).

this case the system acts as a disordered metal so that its resistivity increases slowly with decreasing temperature. To see if electron localization in $KB_6$ originate from a Mott−Hubbard localization, we carried out spin-polarized electronic band structure calculations for $KB_6$ using the APW + lo method as a function of the cell parameter at the fixed spin moments $M$ of 0.0, 0.5, and 1.0 $\mu_B$/FU.

**5.1. Comparison between First Principles and EHTB Calculations.** The band dispersion relations and the density of states of $KB_6$, calculated by the APW + lo method, are shown in Figures 13 and 14, respectively. The top of the valence bands and the bottom of the conduction bands occur at $X$ with a band gap of approximately 1.2 eV. The top portion of the valence bands is dominated by the B 2p orbitals, and the bottom portion of the conduction bands has some contributions from the cations. The valence bands are partially empty for $KB_6$ with 19 valence electrons/FU so that hole carriers are present in $KB_6$. Figure 15 shows the band dispersion relations calculated for $KB_6$ using the EHTB method. The overall band dispersions of $KB_6$ obtained from EHTB calculations are quite similar to those obtained by the APW + lo method. A noticeable difference between the first principles and EHTB calculations is the energy of the top of the partially empty bands at Γ and $R$: this band top at $R$ lies lower than that at Γ in the first principles calculations, but they are nearly the same in energy in the EHTB calculations. The latter is due essentially to the well-known deficiency of the EHTB method that, for systems with

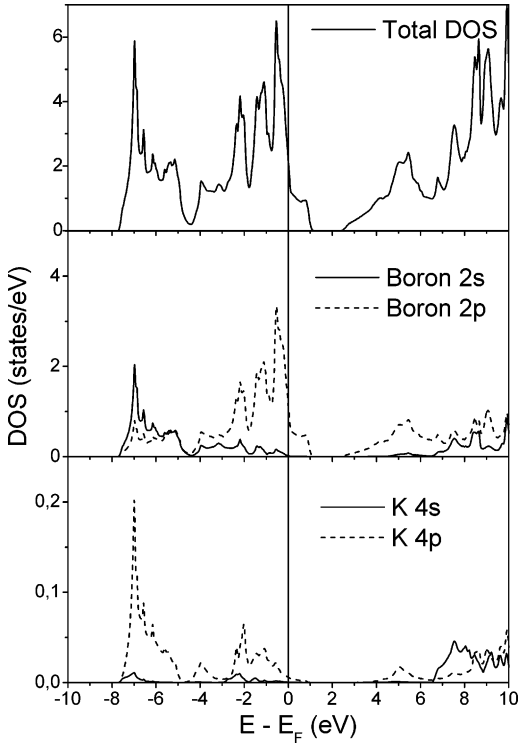


**Figure 14.** Density of states for $KB_6$, with contributions from B and K orbitals, calculated by the APW + lo method.

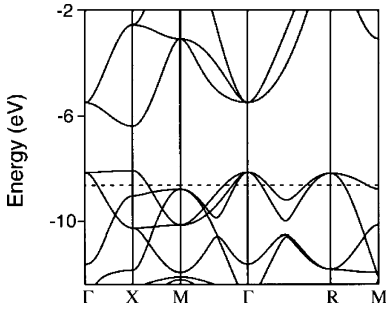


**Figure 15.** Dispersion relations of the electronic band structure of $KB_6$ obtained by EHTB calculations.

$\pi$- and $\sigma$-bonding levels, the $\sigma$-bonding levels are generally placed higher in energy than they ought to be.

**5.2. Nature of the Valence Bands.** To gain insight into the electrical and magnetic properties of $KB_6$, it is necessary to examine the orbital compositions and chemical bonding leading to its partially filled bands. For this purpose we start from chemical bonding considerations and make use of EHTB calculations. This approach is justified because the electronic band structures of $KB_6$ obtained from EHTB calculations are quite similar to those determined by the first principles calculations.

There are two sets of group orbitals of $B_6$ octahedra that contribute to the valence bands of $KB_6$. As shown in Figure 16a, one set consists of three degenerate tangential $\sigma$-bonding orbitals (i.e., $\sigma_{xy}$, $\sigma_{xz}$, and $\sigma_{yz}$) contained in the $B_4$ square planes. In each pair of diagonally opposite corners of a $B_4$ square plane, the B 2p orbitals have opposite signs in these group orbitals. Figure 16b shows the other set of three degenerate $\sigma$-nonbonding orbitals (i.e., $n_x$, $n_y$, and $n_z$) lying on the $x$-, $y$-, and $z$-axes. The group orbitals of a $B_6$

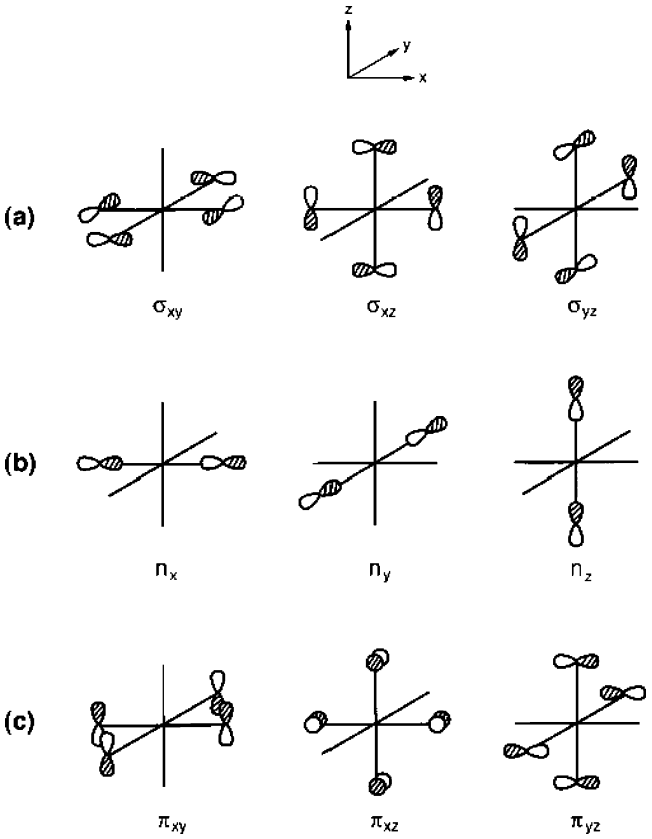


**Figure 16.** Group orbitals of a $B_6$ octahedron leading to the valence and conduction bands of $KB_6$: (a) three degenerate tangential $\sigma$-bonding orbitals; (b) three degenerate $\sigma$-nonbonding orbitals; (c) three degenerate $\pi$-nonbonding orbitals.

octahedron contributing to the conduction bands of $KB_6$ are three degenerate $\pi$-antibonding orbitals (i.e., $\pi_{xy}$, $\pi_{xz}$, and $\pi_{yz}$) contained in the $B_4$ square planes as shown in Figure 16c. In each pair of diagonally opposite corners of a $B_4$ square plane, the B 2p orbitals have an identical sign in these group orbitals. The $\sigma$-bonding orbitals (i.e., $\sigma_{xy}$, $\sigma_{xz}$, and $\sigma_{yz}$) and $\sigma$-nonbonding orbitals (i.e., $n_x$, $n_y$, and $n_z$) lead to the valence and conduction bands of $KB_6$ and the $\pi$-antibonding orbitals (i.e., $\pi_{xy}$, $\pi_{xz}$, and $\pi_{yz}$) to the conduction bands of $KB_6$. The nature of the valence bands is analyzed below.

Each type of the tangential $\sigma$-bonding group orbitals in Figure 16a gives rise to $\pi$-interactions in the two orthogonal directions of the group orbital plane but to a very weak $\pi$-interaction along the direction perpendicular to the group orbital plane. For example, the $\sigma_{xy}$ orbitals lead to $\pi$-interactions along the *x*- and *y*-directions but to a negligible $\pi$-interaction along the *z*-direction. To a first approximation, therefore, three essentially 2D electronic bands result from the three tangential $\sigma$-bonding group orbitals. For convenience, these bands resulting from the $\sigma_{xy}$, $\sigma_{xz}$, and $\sigma_{yz}$ orbitals will be referred to as the $\sigma_{xy}$, $\sigma_{xz}$, and $\sigma_{yz}$ bands, respectively. Figure 17a shows the schematic dispersion relations of the three bands. In each tangential $\sigma$-bonding orbital, the B 2p orbitals located at the diagonally opposite corners have opposite signs. Consequently, between adjacent $B_6$ clusters, the $\sigma_{xy}$ band for example has $\pi$-antibonding along the *x*- and *y*-directions at $\Gamma = (0, 0, 0)$, $\pi$-bonding along the *x*-direction, but $\pi$-antibonding along the *y*-direction at $X = (a^*/2, 0, 0)$ and $\pi$-bonding along the *x*- and *y*-directions at $M = (a^*/2, b^*/2, 0)$. Though not shown in Figure 17a, this band is almost dispersionless along the $\Gamma-Z$ direction, where $Z = (0, 0, c^*/2)$, because $\sigma_{xy}$ group orbitals have very weak $\pi$-interactions along that direction. Thus, as the wave vector varies along one of the $a^*$-, $b^*$-, and $c^*$-directions, two bands show strong dispersions with the remaining one nearly dispersionless.

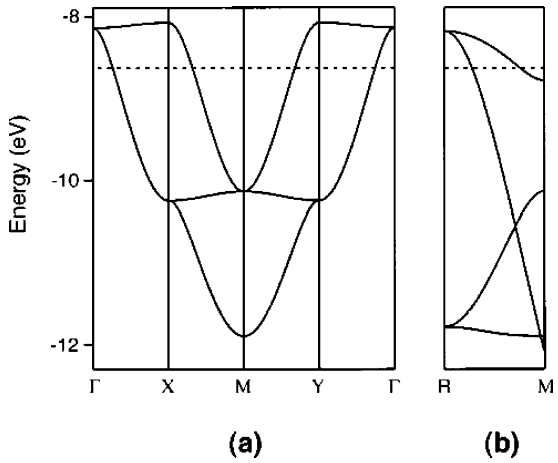


**Figure 17.** Schematic dispersion relations of the valence bands of $KB_6$: (a) the bands resulting from the three tangential $\sigma$-bonding orbitals; (b) those resulting from the three tangential $\sigma$-bonding orbitals and three degenerate $\sigma$-nonbonding orbitals. The wave vector point *Y* refers to $(0, b^*/2, 0)$.

Figure 17b depicts the dispersion relations of the top six filled bands along the $R \rightarrow M$ line, where $R = (a^*/2, b^*/2, c^*/2)$. At *R* the top three triply degenerate levels are derived from the group orbitals $n_x$, $n_y$, and $n_z$, which lie above the next triply degenerate levels from the group orbitals $\sigma_{xy}$, $\sigma_{xz}$, and $\sigma_{yz}$. The $n_x$, $n_y$, and $n_z$ bands become more stable as the wave vector moves away from *R* to *M* and show the same trend along other directions from *R*. Thus, these bands have a 3D character. With 19 valence electrons/unit cell in $KB_6$, the three 2D bands (i.e., the $\sigma_{xy}$, $\sigma_{xz}$, and $\sigma_{yz}$ bands) become partially empty near the top, and so are the three 3D bands (i.e., $n_x$, $n_y$, and $n_z$ bands).

**5.3. Spin-Polarized Electronic Band Structure.** The normal metallic state has no net magnetic moment/FU. The spin-polarized state with nonzero *M* represents the ferromagnetic metallic state that has the net magnetic moment *M*/FU, as can be seen from Figure 18, which shows the DOS plots of the up-spin and down-spin states calculated for $M = 0.5\ \mu_B$/FU. The variations of the total energies of $KB_6$/FU as a function of the cell parameter are summarized in Figure 19, where the relative energies of the total energies were given with the normal metallic state taken as the energy reference. The calculated cell parameter lies within 1% of the experimental value and does not depend on *M*. The spin-polarized state is less stable than the normal metallic state. Nevertheless, the energy difference between the spin-polarized and the normal metallic state is very small for small *M* but increases sharply with increasing *M*.

Our spin-polarized and non-spin-polarized electronic band structure calculations show that $KB_6$ is most stable in the normal metallic state, which is inconsistent with the results of the magnetic susceptibility, EPR, and NMR measurements.

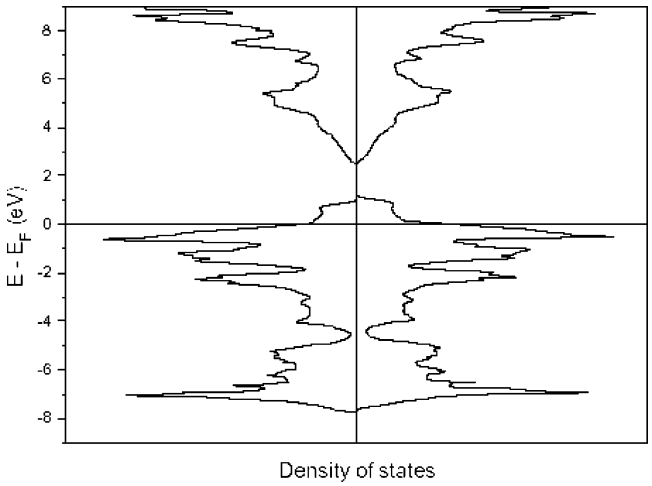


**Figure 18.** DOS plots of the up-spin and down-spin states calculated for $KB_6$ using spin-polarized APW + lo band structure calculations under the constraint of $M = 0.5\ \mu_B$/formula weight.

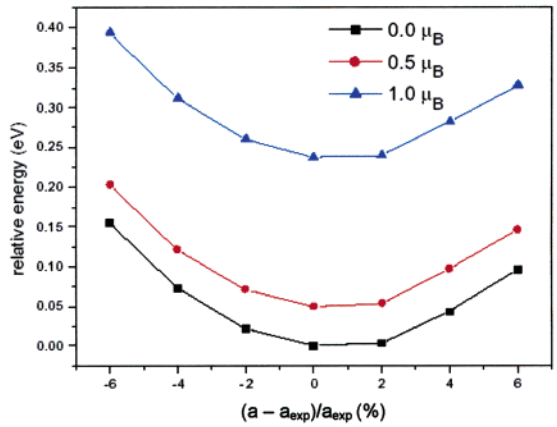


**Figure 19.** Variations of the total energies of $KB_6$/formula unit calculated by APW + lo band structure calculations as a function of the cell parameter, for the nonmagnetic case and for two solutions with constrained magnetic moments.

Therefore, the Mott−Hubbard localization is not responsible for the electron localization in $KB_6$. A probable cause for the electron localization in $KB_6$ will be discussed in section 6.

## 6. Discussion

**6.1. Electron Localization and EPR Signals.** $KB_6$ would be a normal metal if electron localization is absent. The magnetic susceptibility and EPR spectra of $K_{0.97}B_6$ show that it is not a normal metal but has localized electrons. The NMR spectra of $K_{0.97}B_6$ are also consistent with this view. Our electronic band structure calculations indicate that a Mott−Hubbard localization is not responsible for the electron localization in $KB_6$. It should be noted that the electronic band structure calculations assumed no local distortions in $KB_6$ and a stoichiometric sample, whereas the sample is slightly nonstoichiometric, with a significant effect on the $^{11}B$ NMR signal. We now discuss the occurrence of electron localization in $KB_6$ from the viewpoint of local electron−phonon interactions leading to bipolarons.[25]

It is noted that the three valence bands resulting from the group orbitals $\sigma_{xy}$, $\sigma_{xz}$, and $\sigma_{yz}$ are narrow. The bands resulting from the group orbitals $n_x$, $n_y$, and $n_z$ are slightly empty, which can be assumed to be completely occupied for the sake of simplicity. Then, $KB_6$ has five electrons/FU to fill the three $\sigma_{xy}$, $\sigma_{xz}$, and $\sigma_{yz}$ group orbitals. Therefore, each $B_6$ octahedron can adopt one of the three localized electron configurations, i.e., $(\sigma_{xy})^1(\sigma_{xz})^2(\sigma_{yz})^2$, $(\sigma_{xy})^2(\sigma_{xz})^1(\sigma_{yz})^2$, and $(\sigma_{xy})^2(\sigma_{xz})^2(\sigma_{yz})^1$, and is hence subject to a weak Jahn−Teller (JT) instability. The latter should be weak because the occupancy of the triply degenerate level is far from half-filling. From the viewpoint of this local electronic structure, each $B_6$ octahedron can have one unpaired spin. However, most spins of the $B_6$ octahedra in a spin bag are paired up. Thus, it is important to account for why this is the case. The spins of two adjacent $B_6$ octahedra can be antiferromagnetically coupled to form a singlet spin pair if their magnetic orbitals are identical in symmetry and hence overlap substantially.[43] Such a spin dimer is schematically depicted in Figure 20, where each $B_6$ octahedron is represented by a heavy dot (Figure 20a). The overlap between the two magnetic orbitals will lead to bonding and antibonding levels (Figure 20b). With two spins/spin dimer, the bonding level is occupied while the antibonding level is empty, which leads to no unpaired spin. Such singlet spin dimers may be represented by $(\sigma_{xy}-\sigma_{xy})$, $(\sigma_{xz}-\sigma_{xz})$, and $(\sigma_{yz}-\sigma_{yz})$ depending on the symmetry of the magnetic orbitals involved. Such a singlet spin dimer can be further stabilized by a local distortion around it induced by the weak JT instability. The resulting singlet spin dimers are then bipolarons.[25] Such a spin pairing can occur in all three directions of a crystal particle without any long-range order.

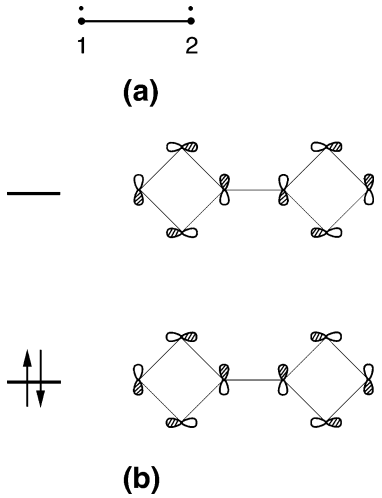


**Figure 20.** (a) Schematic representation of a spin dimer $(\sigma_{xy}-\sigma_{xy})$, $(\sigma_{xz}-\sigma_{xz})$, or $(\sigma_{yz}-\sigma_{yz})$ in $KB_6$. (b) Nodal properties of the bonding and antibonding orbitals of a spin dimer.

**6.2. Spin Pairing and EPR Signals.** The "nucleation" for spin pairing can take place simultaneously at many different parts of a crystal particle. This will leave a small number of "isolated" $B_6$ octahedra (i.e., spin monomers) with no partners to form spin pairs as well as structural units made

(41) Whangbo, M.-H.; Hoffmann, R. *J. Chem. Phys.* **1978**, *68*, 5498.
(42) Ammeter, J.; Bürgi, H.-B.; Thibeault, J.; Hoffmann, R. *J. Am. Chem. Soc.* **1978**, *100*, 3686.
(43) Whangbo, M.-H.; Koo, H.-J.; Dai, D. *J. Solid State Chem.* **2003**, *176*, 417 and references therein.

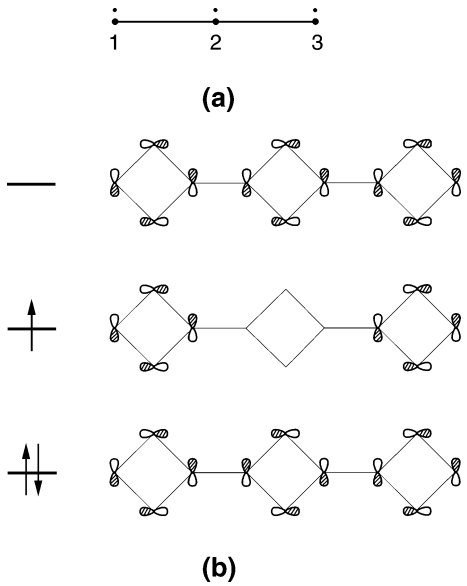


**Figure 21.** (a) Schematic representation of a spin trimer ($\sigma_{xy}-\sigma_{xy}-\sigma_{xy}$), ($\sigma_{xz}-\sigma_{xz}-\sigma_{xz}$), or ($\sigma_{yz}-\sigma_{yz}-\sigma_{yz}$) in $KB_6$. (b) Nodal properties of the bonding, nonbonding, and antibonding orbitals of a spin trimer.

up of three consecutive $B_6$ octahedra in one direction (i.e., spin trimers) (Figure 21). If an unpaired spin resides in one of the $\sigma_{xy}$, $\sigma_{xz}$, and $\sigma_{yz}$ orbitals of a $B_6$ octahedron, the spin density is equally shared among four boron atoms in each $B_6$ octahedron. The analysis of the areas of the narrow EPR peak below 60 K shows that the temperature dependence of the narrow peak follows the Curie−Weiss law. Therefore, we assign the narrow EPR signal to a spin localized in one $B_6$ octahedron. A spin trimer, in which the magnetic orbitals of the three adjacent $B_6$ octahedra have the same symmetry, may be represented by ($\sigma_{xy}-\sigma_{xy}-\sigma_{xy}$), ($\sigma_{xz}-\sigma_{xz}-\sigma_{xz}$), or ($\sigma_{yz}-\sigma_{yz}-\sigma_{yz}$) depending on the symmetry of the magnetic orbitals involved. In such a spin trimer (Figure 21a), the three magnetic orbitals overlap to form bonding, nonbonding, and antibonding orbitals (Figure 21b).[44] With three spins, the bonding level is completely filled and the nonbonding level is singly filled. By symmetry this singly filled level has nonzero orbital component only on the end two $B_6$ octahedra, as shown in Figure 21b. The centers of the end two $B_6$ octahedra in a spin trimer are separated by ~0.85 nm, and the outermost B atoms of the end two $B_6$ octahedra by ~1.10 nm. These distances are of the order of the average distance between adjacent spins (i.e., 1.0 nm) estimated from the $\Delta H_{pp}$ value (310 G) of the broad EPR peak. The temperature-independence of the $\Delta H_{pp}$ value can be readily explained if spin trimers are responsible for the broad EPR peak, because the distance between the spin-carrying $B_6$ octahedra in each spin trimer remains constant regardless of how many spin trimers are present in a spin bag. (For longer linear oligomers such as pentamer and heptamer, which are composed of an odd number of $B_6$ octahedra, the unpaired spin is also contained in the nonbonding level that has no orbital contribution on every second $B_6$ octahedron. Thus, spin-containing $B_6$ octahedra are separated by about 1.0 nm in these oligomers as well. However, spin trimers are more likely to occur than longer spin oligomers, as discussed below.)

**6.3. Local Strains and Hysteresis.** The spin pairing between adjacent $B_6$ octahedra in $KB_6$ leading to singlet spin pairs must cooperate with local JT distortions, which necessarily introduces strained local regions in the lattice. Since $KB_6$ has an isotropic 3D lattice, the strain should be evenly distributed in three directions. Consequently the size of a spin-paired structure should be limited. In principle, one might imagine larger spin singlet units involving even number of $B_6$ octahedra, e.g., ($\sigma_{xy}-\sigma_{xy}-\sigma_{xy}-\sigma_{xy}$), ($\sigma_{xz}-\sigma_{xz}-\sigma_{xz}-\sigma_{xz}$), and ($\sigma_{yz}-\sigma_{yz}-\sigma_{yz}-\sigma_{yz}$). However, such units would introduce a stronger local strain and hence would be energetically unfavorable.

Since each $B_6$ octahedron is connected to six neighboring $B_6$ octahedra by the interoctahedron B−B bonds, a JT distortion of a $B_6$ octahedron should affect the nature of the JT distortions in the neighboring $B_6$ octahedra. This would lead to a cooperative JT distortion to a certain extent and hence to a distribution of stress in the crystallites. The slow relaxation process may be related to the formation and destruction of spin paired units and hence to a redistribution of stress. The hysteresis in the magnetic susceptibility and EPR susceptibility observed below 70 K should be related to how the distributions of the spin paired units and depend on the thermal and magnetic history of the sample. The unit cell parameter of $KB_6$ exhibits an unusual temperature-dependence below 70 K. This behavior may reflect the effect of the stress distribution associated with local JT distortions.

**6.4. Spin Pairing and NMR Signals.** $^{11}B$ NMR shows two signals with some distributions. On the basis of the spin-paring mechanism described above, one might wonder if the two NMR signals are related to the two EPR signals. As already discussed, it is reasonable to regard two different $^{11}B$ NMR signals as reflecting the presence of different boron atoms in their Fermi contact shift, i.e., the presence of boron atoms with different amounts of electron transfer from the surrounding K atoms. The latter is possible because $KB_6$ samples contain K vacancies. As for the EPR, the spin-pair formation and breaking should be dynamic in an ideal situation, and the resulting rearrangement should be very rapid on the NMR time scale (approximately $10^{-6}$ s) so that the two kinds of boron species observed by EPR cannot be distinguished by NMR. However, as discussed above, this rearrangement is relatively slow due to the necessary redistribution of stress in the sample. The presence of K vacancies should, therefore, influence both the patterns of the spin pairing and the speed of the rearrangement process.

## 7. Concluding Remarks

With 19 valence electrons/FU, the valence bands of $KB_6$ are partially filled so that $KB_6$ is predicted to be a normal metal by electronic band structure calculations. However, the electrical resistivity of $KB_6$ shows that it is not a normal metal. The magnetic susceptibility and EPR measurements reveal that $KB_6$ has localized electrons, which is supported by the NMR measurements. The occurrence of electron

(44) Albright, T. A.; Burdett, J. K.; Whangbo, M.-H. *Orbital Interactions in Chemistry*; Wiley: New York, 1985.

localization in $KB_6$ is not explained by a Mott−Hubbard localization but by local electron−phonon interactions leading to bipolarons. The occurrence of singlet spin dimers in $KB_6$ can be understood in terms of the weak JT instability of the $B_6$ octahedra that arises from their localized electron configuration $(\sigma_{xy})^1(\sigma_{xz})^2(\sigma_{yz})^2$, $(\sigma_{xy})^2(\sigma_{xz})^1(\sigma_{yz})^2$, or $(\sigma_{xy})^2(\sigma_{xz})^2(\sigma_{yz})^1$.

The EPR spectra of $KB_6$ exhibit one broad and one narrow overlapping peak. Our analysis indicates that the narrow EPR peak arises from a spin present in the magnetic orbital $\sigma_{xy}$, $\sigma_{xz}$, or $\sigma_{yz}$ orbital of one $B_6$ octahedron, while the broad EPR peak arises from a spin delocalized in a spin trimer $(\sigma_{xy}-\sigma_{xy}-\sigma_{xy})$, $(\sigma_{xz}-\sigma_{xz}-\sigma_{xz})$, or $(\sigma_{yz}-\sigma_{yz}-\sigma_{yz})$. Such a spin trimer has one unpaired electron in the nonbonding orbital that has nonzero orbital coefficients only on the end two $B_6$ octahedra. The distance between the centers of the end two $B_6$ octahedra is of the order of the average distance between adjacent spins estimated from the $\Delta H_{pp}$ value of the broad EPR peak. This assignment explains why the line width $\Delta H_{pp}$ of the broad peak is independent of the EPR frequency.

The temperature-dependence of the magnetic and EPR susceptibility curves of $KB_6$ show a prominent hysteresis below 70 K, and this hysteresis involves a slow relaxation process. The latter should be related to the formation and destruction of spin paired units and hence to a redistribution of the stress arising from local distortions associated with the spin pairing. The unusual temperature dependence of the unit cell parameter below 70 K should reflect the effect of the stress distribution.

**Acknowledgment.** Work at North Carolina State University was supported by the Office of Basic Energy Sciences, Division of Materials Sciences, U.S. Department of Energy, under Grant DE-FG02-86ER45259 (M.-H.W) and Contract W-31-109-Eng-38 (A.I.S.) and also by the NHMFL Visiting Scientist Program (A.I.S). The computational work at ICMCB was aided by the M3PEC project (Modélisation Microscopique et Mésoscopique en Physique, dans l'Environnement et en Chimie), Université de Bordeaux I. We gratefully thank D. Massiot and P. Florian for initiating the NMR work at CRMHT (Orléans, France), J.-M. Bassat, R. Decourt, and B. Guillaume from ICMCB for their technical assistance, and L. C. Brunel, J. van Tol, and A. Ozarowski at NHFML for assistance in quasi-optical EPR experiments.

IC049444C